Chinese Chemical Letters 37 (2026) 111318

Contents lists available at ScienceDirect

Chinese Chemical Letters

journal homepage: www.elsevier.com/locate/cclet

Discovery of α-mangostin derivatives as novel PDE4 inhibitors for the treatment of Alzheimer's disease: An artificial intelligence-driven synergized strategy

Zhi-Pei Sang[a,1], Teng Xue[a,1], Qian-Ru Xing[a,1], Qi-Yao Zhang[a], Hong-Song Chen[b], Xue Wang[a], Fu-Rong Zhang[a], Wen-Ling Fu[a], Wu Dong[b], Shu-Heng Huang[a,*], Yi-You Huang[a,*], Hai-Bin Luo[a,c,*]

[a] *Key Laboratory of Tropical Biological Resources of Ministry of Education and Hainan Engineering Research Center for Drug Screening and Evaluation, School of Pharmaceutical Sciences, Hainan University, Haikou 570228, China*
[b] *College of Animal Science and Technology. Inner Mongolia Minzu University, Tongliao 028000, China*
[c] *Song Li's Academician Workstation of Hainan University (School of Pharmaceutical Sciences), Yazhou Bay, Sanya 572000, China*

ARTICLE INFO

Article history:
Received 6 February 2025
Revised 13 May 2025
Accepted 14 May 2025
Available online 16 May 2025

Keywords:
Alzheimer's disease
Generative recurrent neural network
α-Mangostin
PDE4 inhibitor
In vivo study

ABSTRACT

Alzheimer's disease (AD) is a chronic, progressive neurodegenerative disorder with no effective therapeutic agents currently available. Inhibiting phosphodiesterase 4 (PDE4) has emerged as a promising strategy for AD treatment. In this study, we employed a synergistic approach combining generative recurrent neural network (RNN)-driven combinatorial compound design, virtual screening, and structure-activity relationship (SAR) analysis to discover novel PDE4 inhibitors. Utilizing α-mangostin as a hit compound (half maximal inhibitory concentration (IC_{50}) = 1.31 μmol/L), we identified a novel PDE4 inhibitor, **13d** (IC_{50} = 72.8 nmol/L) with moderate liver microsomal stability (rat liver microsomes (RLM), $t_{1/2}$ = 32.4 min). *In vitro* activity results indicated that **13d** exhibited favorable anti-inflammatory effects and promising neuroprotective activity. *In vivo* experiments demonstrated that **13d** significantly improved $AlCl_3$-induced zebrafish AD model by inhibiting PDE4 and reducing inflammatory cytokine. Further, **13d** significantly alleviated $AlCl_3$/D-galactose-induced AD mouse model. These findings highlight the potent PDE4 inhibitor **13d** with promising anti-AD activity, underscoring the potential of artificial intelligence-driven drug discovery for novel therapeutic agents for AD.

© 2026 Published by Elsevier B.V. on behalf of Chinese Chemical Society and Institute of Materia Medica, Chinese Academy of Medical Sciences.

Alzheimer's disease (AD) is a progressive neurodegenerative disorder characterized by deteriorating memory, declining language skills, and a spectrum of cognitive impairments in older adults [1]. Currently, over 55 million individuals worldwide are diagnosed with AD, and this number is projected to reach 139 million by 2050 [2]. The disease poses significant social and economic challenges. Currently available Food and Drug Administration (FDA)-approved treatments include cholinesterase inhibitors (such as rivastigmine, donepezil, and galantamine), *N*-methyl-D-aspartic acid (NMDA) receptor antagonists (like memantine), and monoclonal antibodies (including aducanumab and lecanemab). Although these therapies offer limited symptomatic relief, they do not stop, delay, or reverse the progression of the disease [3]. Additionally, many patients experience substantial adverse effects, including gastrointestinal disturbances, dizziness, heart failure, seizures, and infusion-related reactions associated with monoclonal antibodies [4–7]. Therefore, the search for effective treatments has become an urgent priority.

Phosphodiesterase IV (PDE4) which specifically hydrolyzes cAMP (cyclic adenosine monophosphate), has four isoforms (PDE4A, PDE4B, PDE4C, and PDE4D), and is widely expressed in the brain of demented patients [8–10]. Since the 1990s, many reports have confirmed that PDE4 inhibitors (such as roflumilast [11], rolipram [12], HT-0712 [8], and FFPM [13]) could significantly improve learning and memory through cAMP/cAMP-response element binding protein (CREB)/brain derived neurotrophic factor (BDNF) and anti-inflammatory effects. By increasing intracellular cAMP levels, PDE4 inhibitors enhance CREB phosphorylation, which in turn upregulates the expression of BDNF, a crucial neurotrophic factor involved in synaptic plasticity, neuronal survival, and memory formation. This neuroprotective mechanism con-

* Corresponding authors.
E-mail addresses: shhuang@hainanu.edu.cn (S.-H. Huang), hyyou@hainanu.edu.cn (Y.-Y. Huang), hbluo@hainanu.edu.cn (H.-B. Luo).
[1] These authors contributed equally to this work.

https://doi.org/10.1016/j.cclet.2025.111318
1001-8417/© 2026 Published by Elsevier B.V. on behalf of Chinese Chemical Society and Institute of Materia Medica, Chinese Academy of Medical Sciences.

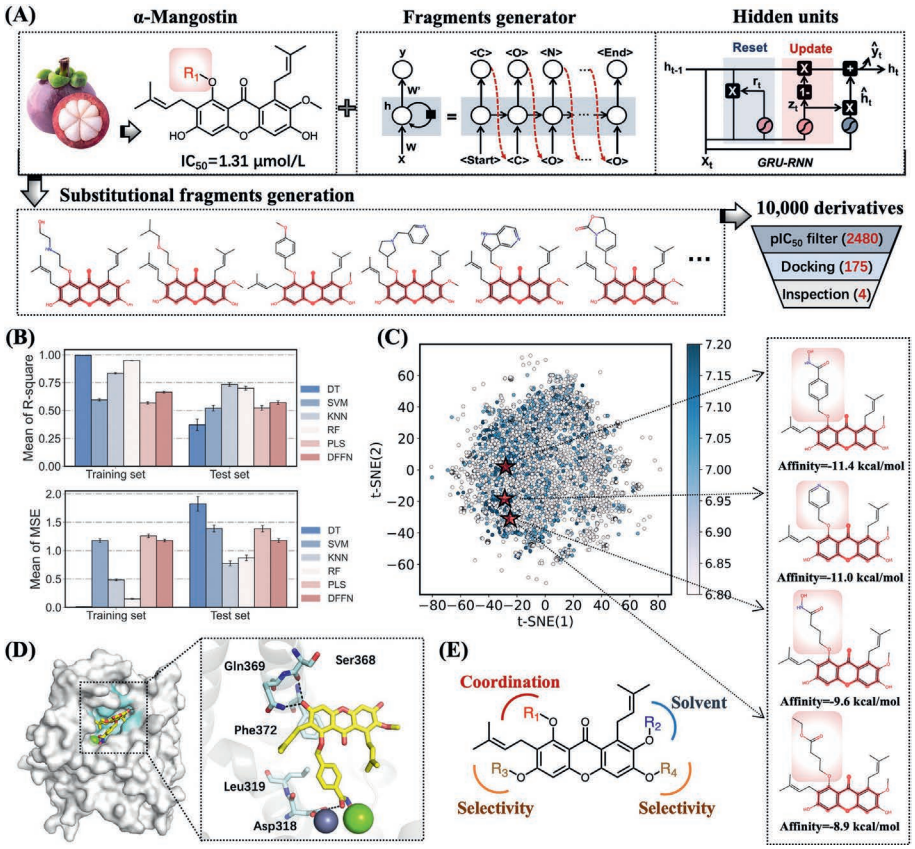


Fig. 1. Discovery of novel α-M derivatives as lead compounds. (A) Schematic illustration of the molecular design and development of noval α-M derivatives. (B) The performance of the 5 ML models and the DFNN model on the training and test dataset. Default parameters were used for the ML models if not specified. (C) The distribution in the chemical space of the 10,000 generated α-M derivatives. (D) Binding modes of representative compound, where key residues were represented as stick models. The H-bond interactions were indicated by black dashed lines. (E) General modification methods of structure-based molecular design.

tributes to reduced neuronal apoptosis, mitigates neuroinflammation, and counteracts oxidative stress [8,9]. More importantly, PDE4 inhibitors have had positive results in clinical studies, such as, roflumilast has completed Phase II clinical trials (NCT04658654, NCT01433666) investigating cognitive-related outcomes [14,15], BPN14770 is currently undergoing Phase II clinical trials for AD (NCT03817684), and HT-0712 has completed Phase II clinical trials (NCT02013310) targeting age-related memory impairment [8,9]. Therefore, PDE4 as a target for AD has received widespread attention.

α-Mangostin (α-M, Fig. 1A) is a major polyphenolic xanthone extracted from the pericarps, bark, and dried sap of the mangosteen fruit (*Garcinia mangostana* L.), first isolated in 1855. Traditionally employed in Southeast Asian medicine, α-M has gained substantial research interest for its multifaceted biological activities [16,17]. Notably, emerging evidence indicates its potential in mitigating cognitive decline and providing neuroprotection in AD, attributed to its powerful antioxidant, anti-inflammatory, and neuroprotective properties [18]. In our group's preliminary work, we discovered α-M as a natural PDE4 inhibitor (half maximal inhibitory concentration (IC_{50}) = 1.31 μmol/L) [19], warranting further development into a potent PDE4 inhibitor for the treatment of AD.

Traditional drug discovery processes, particularly in medicinal chemistry, are often characterized by a degree of blindness and unpredictability. Due to the vastness of chemical space and the inherent complexity of molecular interactions, it is difficult to comprehensively explore all possible compounds and their corresponding biological activities [20,21]. This limitation leads to inefficiencies and high costs in the drug development pipeline. However, with the rapid advancement of artificial intelligence (AI) and machine learning (ML) technologies, new opportunities have emerged to overcome these challenges. Integrating generative models with virtual screening techniques enables a more systematic and efficient exploration of the chemical space [22,23]. This combination of AI-driven approaches significantly enhances the efficiency of drug discovery, reducing both the time and resources required to identify viable drug candidates.

Herein, we present a novel approach that combines generative recurrent neural network (RNN)-driven combinatorial compound design, virtual screening, and structure-activity relationship (SAR) analysis for the *de novo* design of PDE4 inhibitors and the evaluation of their potential anti-AD activity. This integrated strategy synergistically combines the strengths of AI-powered molecular generation with traditional medicinal chemistry principles, enabling systematic exploration of chemical space. The synergistic strategy consists of the following steps: The synergized strategy for the intelligent drug design of PDE4 inhibitors is as follow: (1) Generating 10,000 unique substitutional fragments by RNN-based "Fragment Generator"; (2) Constructing a virtual library of α-M derivatives by substituent modification; (3) Virtual screening of PDE4 inhibitors by ML modeling and molecular docking; (4) Optimizing the lead compounds by SAR studies; (5) Evaluating the anti-AD of **13d** *in vitro* and *in vivo* experiments (Fig. 1A). By using this strategy, we discovered a novel PDE4 inhibitor, designated as compound **13d** ($IC_{50} = 72.8 \pm 9.6$ nmol/L). The significant efficacy of **13d** warranted comprehensive investigations into its drug-likeness profile. *In vivo* studies were conducted using $AlCl_3$-induced zebrafish AD model and $AlCl_3$/galactose-induced mice. These findings represent a substantial advancement in the design and development of

potent PDE4 inhibitors, positioning compound **13d** as a promising lead for the treatment of AD.

To fully explore the chemical space of α-M derivatives, we first utilized a self-built RNN-based "Fragment Generator" to generate 10,000 substituent fragments [24]. To optimize the generation of small molecular substituents, we curated a specialized training set from ChEMBL consisting of 1179,477 unique drug-like molecules (MW $<$ 200 Da). After 30,000 training steps, the loss value converged and plateaued at 23.1, while the validity rate of the generated SMILES strings reached 93.4% (Fig. S1 in Supporting information), demonstrating the model's capability to consistently produce structurally valid molecular fragments. Then, 10,000 fragments were systematically substituted onto the α-M scaffold at the R_1 position constructing a virtual library of α-M derivatives, thereby maximizing structural diversity. Subsequently, for developing a reliable ML model for predicting PDE4 inhibitory activities, we evaluated the performance of five ML algorithms, *i.e.*, decision tree (DT), support vector machine (SVM), k-nearest neighbor (K-NN), random forest (RF), partial least squares (PLS), along with the deep learning model deep feedforward neural network (DFNN). Based on prediction accuracy and balanced performance on the test set, K-NN was selected as the optimal model, with R^2 of 0.83 and 0.73 on the training and test set, respectively (Fig. 1B). Then, the virtual library was subjected to activity prediction using the optimal activity predictor model, which identified 2480 compounds with predicted pIC_{50} values greater than 7, implying strong activity in the nanomolar range (Fig. 1C).

A high-throughput virtual screening method was used to perform molecular docking on the screened compounds. Based on the docking results, 175 compounds with affinities lower than −8 kcal/mol were selected as high-affinity candidates. A synthetic feasibility assessment was then conducted to ensure the practicality of these compounds. Finally, four lead structures with favorable binding modes and high synthetic feasibility were selected for subsequent chemical synthesis and SAR studies. It is noteworthy that molecular docking studies revealed a binding mode similar to that observed in the previously reported crystal structure of PDE4 in complex with α-M derivative (PDB: 6KJZ) [19]. It can be observed the α-M's scaffold embedded well into the catalytic pocket of PDE4, with its benzene fragment forming a π-π stacking interaction with Phe372. In addition, the catalytic site contained a metal binding pocket composed of residues such as Asp318 and Leu319, which formed hydrogen bonds and metal coordination interactions with the R_1 side chain. The R_2 substituent was mainly involved in the solvation region. The R_3 and R_4 substituents respectively extend into the Q1 and Q2 pockets, which are unique subpockets present among PDE4 isoforms, thereby contributing to enhanced selectivity (Figs. 1D and E) [19].

To further optimize the hit structure, we performed structure-based drug design based on the docking results. As shown in Fig. 1E, the R_1 position was suitable for introducing long-chain charged groups, while the R_2 position was modified with CH_3O group. The R_3 and R_4 positions were tailored to enhance the selectivity of PDE4 inhibitors. Subsequently, we designed a series of α-M derivatives by modifying the R_1 position with four selected high-scoring fragments (*i.e.*, pyridine, carboxylic ester, carboxylic acid and hydroximic acid) (Fig. 1C). In consideration of the synthetic accessibility and potential for systematic structural diversification, the second compound was selected as our initial optimization starting point. A total of 22 compounds were synthesized and evaluated for their anti-PDE4 activity.

The synthetic routes for the novel target derivatives **6a**, **6b**, **8a**–**8f**, **11a**–**11c**, **13a**–**13d**, **19a**–**19c** and **20a**–**20d** were illustrated in Schemes S1–S4 (Supporting information).

In order to evaluate the PDE4 inhibitory potency of the target derivatives, liquid scintillation cocktail assay was used, and rolipram was also tested as a positive control [24,25]. Considering cost and efficiency, the PDE4 inhibitory activity of all target compounds was assessed using single-point inhibition tests at concentrations of 1 μmol/L and 100 nmol/L, respectively. As shown in Table 1, both the two alkoxy side chains R_1/R_2 and the targeting metal region fragment significantly influenced the PDE4 inhibitory activity. When the targeting metal region fragment was pyridine, compounds **6a** and **6b** were synthesized by introducing different R_1/R_2 fragments based on our previous work, the results demonstrated that compounds **6a** and **6b** did not exhibit a significant improvement in PDE4 inhibitory activity compared to α-M. When R_1 and R_2 were substituted by the same fragments, compounds **8a**–**8f** were obtained, the PDE4 inhibition data displayed that smaller R_1/R_2 fragments showed better PDE4 inhibitory activity, such as **8b** (methyl fragment), **8d** (ethyl fragment), **8e** (isobutyl), and **8f** (cyclopentyl). Notably, compound **8b**, which contained two methoxy groups, exhibited good PDE4 inhibitory activity at 100 nmol/L (52.76%).

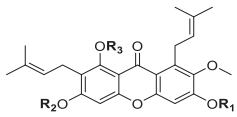
Furthermore, when both alkoxy groups R_1/R_2 were methoxy, we synthesized target compounds **11a**–**11c** and **13a**–**13d** (Table 1), and investigated the influence of carboxylic acid and hydroxamic acid fragments on PDE4 inhibitory activity. The test results showed that derivatives containing carboxylic acid fragments, such as **11a**–**11c**, significantly reduced PDE4 inhibitory activity, with no obvious effect of CH_2 chain length on PDE4 inhibition. After substituting the carboxylic acid fragment of compounds **11a–11c** with hydroxamic acid, derivatives **13a**–**13c** were obtained, the PDE4 inhibitory activity remarkably improved, with no evident influence of CH_2 chain length on inhibition. When the aliphatic chain of compounds **13a**–**13c** was replaced by a benzene ring, derivative **13d** was obtained. Compound **13d** exhibited significantly enhanced PDE4 inhibitory activity, showing 81.75% inhibition at 100 nmol/L with an IC_{50} of 72.8 ± 9.6 nmol/L (Table S1 in Supporting information), outperforming the positive control rolipram (55.74% inhibition at 800 nmol/L).

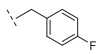
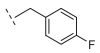
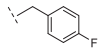
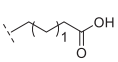
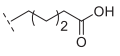
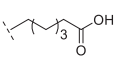
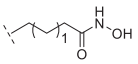
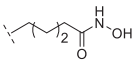
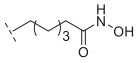
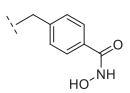
To further discuss the SAR, we removed the isopentene group fragments from **11a**–**11c** and **13a**–**13d**, yielding derivatives **19a**–**19c** and **20a**–**20d** (Table S2 in Supporting information), which exhibited potent PDE4 inhibitory activity. And among derivatives **19a**–**19c** and **20a**–**20d**, derivatives containing hydroxamic acids demonstrated better PDE4 inhibitory activity. Thus, **13d** gave better PDE4 inhibitory potency. The selectivity of compound **13d** across other PDEs was also tested and listed in Table S1. **13d** indicated very weak inhibitory potencies against PDE1C2, PDE3A and PDE8A1, PDE9A, and PDE10A with IC_{50} values higher than 10 μmol/L and selectivity folds greater than 136. Besides, the IC_{50} values of **13d** against PDE2A, PDE7A1 and PDE9A2 were tested to be 1727, 300 and 3442 nmol/L with 23-, 4- and 47-fold selectivity, respectively. Therefore, **13d** was a highly effective and selective PDE4 inhibitor, deserving for further investigations.

To investigate the binding mechanism of **13d** with PDE4, 50-ns molecular dynamics (MD) simulations were performed using the **13d**-PDE4 complex, followed by binding free energy calculations to assess binding affinity. The system remained stable over 50 ns, with the RMSD below 2 Å in the final 20 ns, indicating stable binding. **13d** interacted with active pocket of PDE4 and fitted into a hydrophobic pocket. The total binding free energy was -11.27 ± 14.12 kcal/mol, with van der Waals interactions playing a particularly significant role (-46.15 ± 15.41 kcal/mol). The benzamide formed hydrogen bonds with Thr271 and Asp272, and had π-π conjugation with Phe372, which was the key catalytic residue of PDE4 (-3.48 ± 0.20 kcal/mol). Moreover, van der Walls interactions could be observed between the **13d** and Met273, Ile336, Ser368 and Tyr375 (Fig. S2 in Supporting information).

Before subjected to *in vitro* and *in vivo* pharmacodynamics (PD) studies, pharmacokinetic profile, drug-like property, and acute

Table 1
The PDE4 inhibitory activities of target compounds **6a**, **6b**, **8a–8f**, **11a–11c** and **13a–13d**.



Comp.	R_1	R_2	R_3	PDE4D inhibition rate (%)	
				1 μmol/L	100 nmol/L
6a		CH_3		28.51 %	4.32 %
6b				30.34 %	1.85 %
8a				30.98 %	0.65 %
8b	CH_3	CH_3		70.21 %	52.76 %
8c				8.44 %	-
8d				81.33 %	26.49 %
8e				82.74 %	41.57 %
8f				85.25 %	25.60 %
11a	CH_3	CH_3		56.09 %	2.50 %
11b	CH_3	CH_3		44.82 %	2.91 %
11c	CH_3	CH_3		41.40 %	0.97 %
13a	CH_3	CH_3		94.88 %	44.13 %
13b	CH_3	CH_3		97.85 %	51.30 %
13c	CH_3	CH_3		96.52 %	48.04 %
13d	CH_3	CH_3		99.72 %	81.75 %

safety of **13d** were also evaluated. Liquid chromatograph/mass spectrometer (LC-MS/MS) analysis results demonstrated that **13d** indicated moderate metabolic stability (rat liver microsomes (RLM), $t_{1/2} = 32.4$ min) [26]. The pharmacokinetic properties of compound **13d** were listed in Table S3 (Supporting information). Compound **13d** displayed significant half-lives of 6.5 h (intravenous (i.v.)) and 3.7 h (per oral (p.o.)) and exhibited potent systemic exposure with area under the curve (AUC) values of 1439.0 h ng mL^{-1} (i.v., 2.5 mg/kg) and 68.9 h ng mL^{-1} (p.o., 5.0 mg/kg). The oral bioavailability of **13d** was 2.77 %. To establish the safety profile of **13d**, twenty C57BL/6T (18–22 g) mice (half males and half females) were divided into control and **13d** (500 mg/kg) group, which were administered orally and intragastric for 14 days. Animal studies were conducted in accordance with the approved protocol by the Animal Ethics Committee of Hainan University (approval No. HPIACUC2024090). The results showed that there were not significant changes in movement behavior, mental state, and body weight. Therefore, compound **13d** indicated a favorable safety profile.

The $AlCl_3$-induced zebrafish AD model has been widely applied for the high-throughput screening of novel anti-Alzheimer's agents [27–29]. Herein, we first assessed the safety profile of **13d** through five different concentrations (10.0, 20.0, 40.0, 80.0 and 160.0 μg/mL) in a zebrafish model (Fig. S3 in Supporting information). Notably, no mortality was observed at 160.0 μg/mL over a 120 h exposure period (Fig. S3A). Following this, Fig. S3B showed that **13d** showed significant changes in pericardial edema/body length at 160.0 μg/mL. Moreover, Figs. S3C and D exhibited that 160.0 μg/mL produced obvious influence in swim bladder area. Thus, the maximum tolerable concentration (MTC) of **13d** was 80.0 μg/mL.

Compound **13d** was selected to evaluate its anti-inflammatory activity by assessing the production of nitric oxide (NO), interleukin 6 (IL-6), IL-1β, and tumor necrosis factor-α (TNF-α) in lipopolysaccharide (LPS)-induced BV-2 microglial cells [30]. As shown in Fig. 2A, **13d** did not show obvious cytotoxicity at 10.0 μmol/L, suggesting a favorable safety profile. As illustrated in Figs.

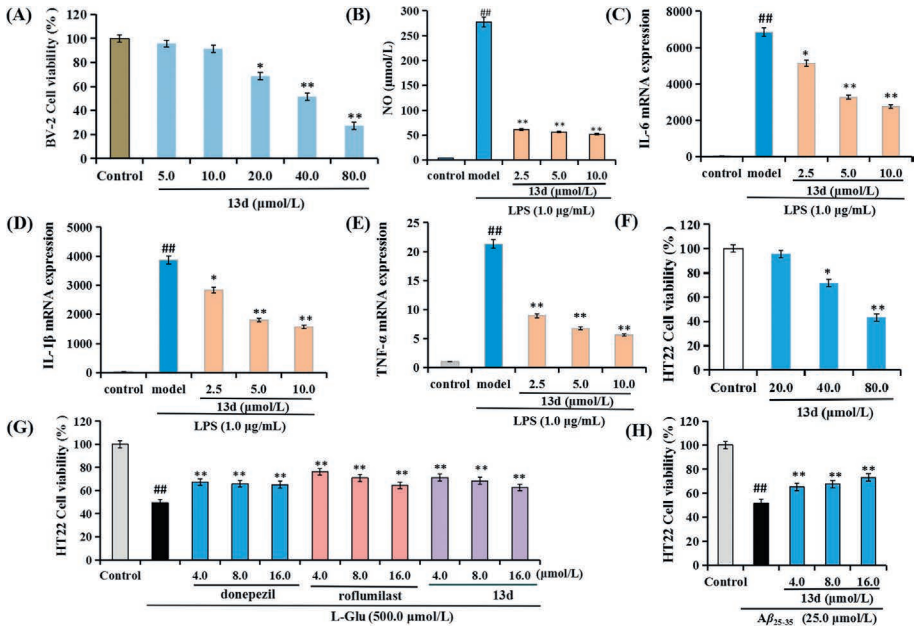


Fig. 2. Anti-inflammatory activities and neuroprotective effects of compound **13d**. (A) The cell viability of **13d** on BV-2 cells was assessed using the CCK-8 assay. $^{*}P < 0.05$, $^{**}P < 0.01$ *vs.* control group. Anti-inflammation effects of **13d** in LPS-stimulated BV-2 cells. (B) NO release. (C) IL-6 mRNA expression. (D) IL-1β mRNA expression. (E) TNF-α mRNA expression. $^{\#\#}P < 0.01$ *vs.* control group. $^{**}P < 0.01$ *vs.* LPS-induced group. (F) Cell viability (%) of **13d** in HT22 cells. $^{*}P < 0.05$, $^{**}P < 0.01$ *vs.* control group. (G) Neuroprotective effects of **13d**, donepezil and roflumilast on Glu-induced HT22 cells injury. (H) Neuroprotective effects of **13d** on Aβ_{25-35}-induced HT22 cells injury. Values were expressed as mean ± SD from three independent experiments. $^{\#\#}P < 0.01$ *vs.* control group. $^{*}P < 0.05$, $^{**}P < 0.01$ *vs.* Glu/Aβ_{25-35}-induced group.

2B–E, **13d** significantly reduced the production of NO, IL-6, IL-1β, and TNF-α in a dose-dependent manner, suggesting that **13d** demonstrated significant anti-inflammatory property.

The neuroprotective effects of **13d** were evaluated in glutamic (Glu)-/Aβ_{25-35}-induced HT22 cell injury using the cell counting kit-8 (CCK-8) assay, with donepezil and roflumilast as positive control [30,31]. As shown in Fig. 2F, **13d** did not produce obvious cytotoxicity in HT22 cells at 20 μmol/L. Fig. 2G illustrated that exposure to 500.0 μmol/L-glutamic acid (L-Glu) significantly decreased cell viability to 49.4% ($P < 0.01$). In contrast, treatment with various concentrations of **13d** (4.0, 8.0, and 16.0 μmol/L) resulted in a significant dose-dependent increase in cell viability, indicating that the neuroprotective potential of **13d** was similar with donepezil and roflumilast. Furthermore, as demonstrated in Fig. 2H, compound **13d** provided significant neuroprotection against Aβ_{25-35}-induced HT22 cells injury in a dose-dependent manner. Thus, these data demonstrated that **13d** presented significant neuroprotective effects against Glu- and Aβ_{25-35}-induced cellular injury.

Based on the MTC of 80.0 μg/mL (136 μmol/L) for **13d**, we subsequently selected three lower concentrations (34.0, 68.0, and 136 μmol/L) for further evaluation following preliminary screening [30,31]. To assess the therapeutic effects of these treatments, a series of behavioral tests were conducted under alternating light and dark conditions over a 60-min period (Fig. 3A). The experimental design included seven groups: control group, **13d** treatment group (136.0 μmol/L), $AlCl_3$-induced model group (140.0 μmol/L), $AlCl_3$ + donepezil (8.0 μmol/L) group, and $AlCl_3$ + **13d** (34.0, 68.0, and 136.0 μmol/L) treatment groups. As indicated in Fig. S4 (Supporting information), zebrafish exposed to $AlCl_3$ demonstrated a statistically significant reduction in swimming speed compared to the control group under light and dark conditions (Figs. S4A–C). In contrast, when treatment with donepezil (8.0 μmol/L), the swimming speed significantly increased. And when treating with **13d** (34.0, 68.0, and 136.0 μmol/L), the swimming speed presented remarkably improved in a dose-dependent manner. Furthermore, Figs. S4D–F showed that **13d** (34.0, 68.0, and 136.0 μmol/L) significantly decreased swimming distance in a dose-dependent manner under the light condition. However, in a dark environment, **13d** exhibited an increasing trend, although no significant differences were observed. Further, when the dark environment was transitioned to a light environment, both donepezil and **13d** significantly improved reaction capacity. When the light environment was switched back to a dark environment, the reaction capacity of **13d** (136.0 μmol/L) was significantly enhanced (Figs. S4G–H). Moreover, the terminal deoxynucleotidyl transferase dUTP nick-end labeling (TUNEL) staining results in Figs. 3B and C displayed that donepezil (8.0 μmol/L) and **13d** (34.0, 68.0, and 136.0 μmol/L) significantly reduced the number of apoptotic cells, compared to model group.

The anti-AD mechanism of compound **13d** was investigated in Figs. 3D–N. Figs. 3D–J indicated that **13d** elevated cAMP levels by inhibiting PDE4A, PDE4B and PDE4D, and further improved the levels of CREB and BDNF. Moreover, **13d** demonstrated significant anti-inflammatory properties by decreasing levels of TNF-α (Fig. 3K), IL-6 (Fig. 3L) and IL-1β (Fig. 3M). Additionally, the APP levels significantly increased in $AlCl_3$ induced neurotoxicity mouse model [32,33]. As displayed in Fig. 3N, **13d** was found to lower amyloid precursor protein (APP) levels in a dose-dependent manner, the possible reason was that **13d** indirectly affected APP expression and metabolism by increasing cAMP levels and anti-inflammatory effects. These results demonstrated that **13d** significantly ameliorated the $AlCl_3$-induced zebrafish AD model *via* PDE4A/4B-mediated cAMP/CREB/BDNF signaling. This signaling pathway facilitated the neuroprotective, anti-apoptotic, and anti-inflammatory actions of **13d**, which collectively decreased the levels of APP and enhanced its behavioral outcomes.

To further evaluate the *in vivo* effects of compound **13d**, the $AlCl_3$ and D-galactose-induced AD mouse model was applied [34,35]. The AD model was established using $AlCl_3$ (20.0 mg/kg) in combination with D-galactose (120.0 mg/kg). $AlCl_3$ was administered *via* oral gavage at a dose of 0.1 mL/10.0 g daily, and D-galactose was injected intraperitoneally at a dose of 0.1 mL/10.0 g. Mice in the normal control group received an equal volume of carboxymethylcellulose sodium (CMC–Na) (0.1 mL/10.0 g). The model-

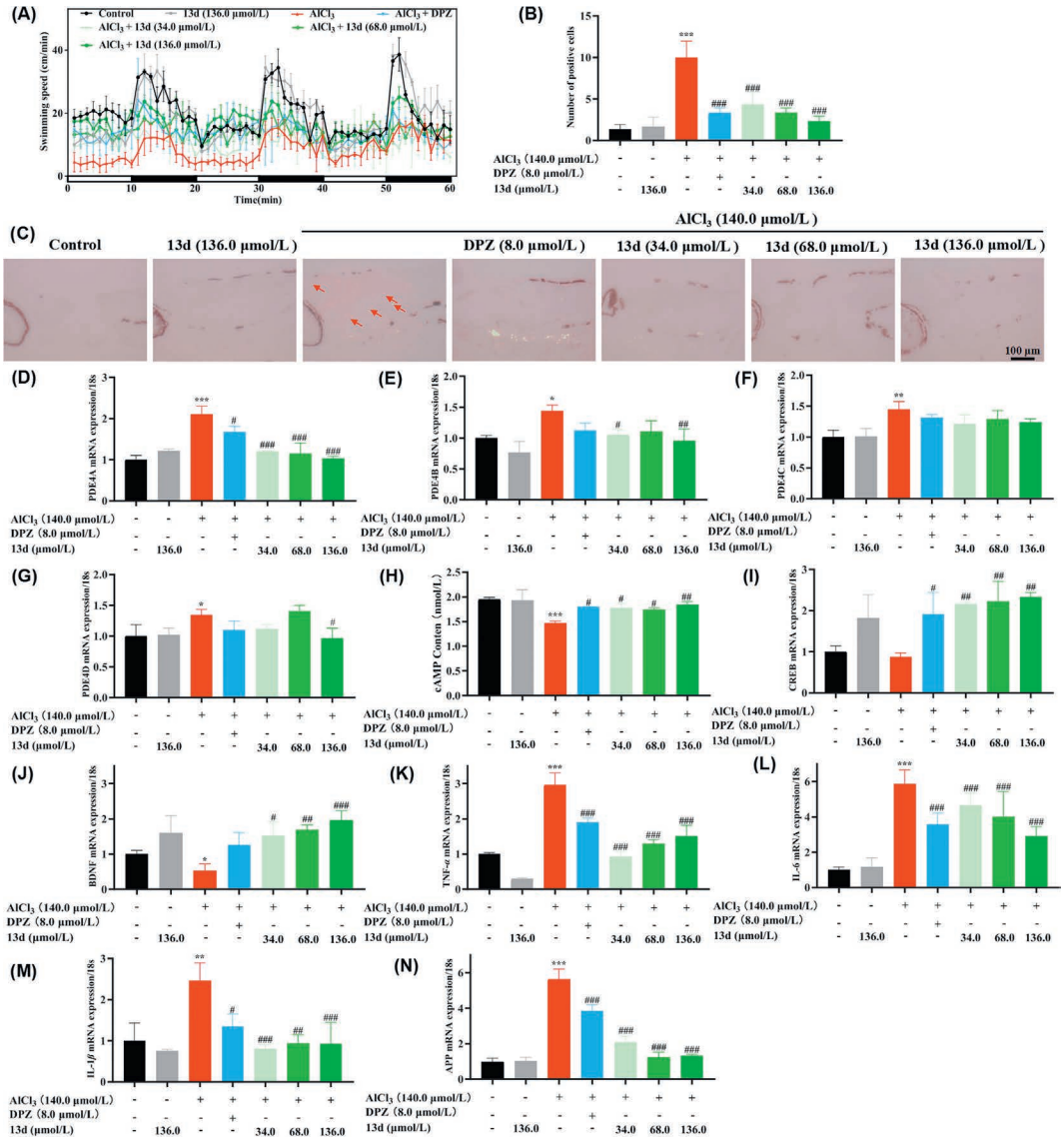


Fig. 3. (A) Behavioral changes in the zebrafish larvae per minute. (B) The apoptotic body/normal cells in the various zebrafish models was statistically analyzed after TUNEL staining. (C) Apoptotic body changes in the brain of zebrafish were performed using TUNEL staining. Scale bar: 10 μm. (D) PDE4A mRNA expression change. (E) PDE4B mRNA expression changes. (F) PDE4C mRNA expression changes. (G) PDE4D mRNA expression changes. (H) cAMP level changes. (I) CREB mRNA expression changes. (J) BDNF mRNA expression changes. (K) TNF-α mRNA expression changes. (L) IL-6 mRNA expression changes. (M) IL-1β mRNA expression changes. (N) APP mRNA expression changes. Values are expressed as mean ± SD from three independent experiments. $^{*}P < 0.05$, $^{***}P < 0.01$, $^{***}P < 0.001$ *vs.* control group. $^{\#}P < 0.05$, $^{\#\#}P < 0.01$, $^{\#\#\#}P < 0.001$ *vs.* $AlCl_3$-induced zebrafish model.

ing was conducted over a continuous period of 60 days. C57BL/6T mice were randomly divided into five groups based on body weight, with each group consisting of 11 mice. The groups included normal control group, model group, positive drug group (3.0 mg/kg donepezil), and **13d** groups (3.0 and 6.0 mg/kg). On the 31st day of modeling, each group was administered orally and intragastric the corresponding treatment at a volume of 0.1 mL/10.0 g, with the normal control and model groups receiving an equal volume of CMC–Na (0.1 mL/10.0 g). Treatment was administered once daily for a total of 30 days. Behavioral tests were subsequently conducted, including the open field test (OFT), novel object recognition test (NOR), and Morris water maze (MWM) (Fig. 4A). As shown in Fig. 4B, there were no significant differences in body weight among the different groups of mice. Fig. 4C demonstrated that **13d** (6.0 mg/kg) and donepezil significantly improved the times cross zones in the open field test. Fig. 4D indicated **13d** (6.0 mg/kg) and donepezil could increase the discrimination index in the NOR test. Fig. 4E exhibited that donepezil and **13d** could decrease the locational navigation escape latency compared with the model group in the MWM test. Moreover, Fig. 4F suggested that **13d**, especially the dose of 6.0 mg/kg, significantly reduced the spatial exploration escape latency ($P < 0.05$). Furthermore, Figs. 4G and H demonstrated that 6.0 mg/kg **13d** remarkably improved spatial exploration shuttle platform ($P < 0.05$), average speed ($P < 0.05$), and the quadrant dwell time in spatial exploration ($P < 0.01$), respectively. And the localized cruise heat map (Fig. 4I) was consistent with the results. Additionally, Figs. S5A–F (Supporting information) exhibited that there were no significant differences observed in the weights of the heart, liver, and kidneys, nor in the levels of CREA (creatinine) and UREA. Therefore, these observations and data indicated that compound **13d** (6.0 mg/kg) significantly enhanced spatial memory and cognitive function. Further, to confirm whether compound **13d** could cross the blood-brain barrier, we measured the concentrations of **13d** in the cerebral cortex and plasma of the high (6.0 mg/kg) dose group. LC-MS analysis indicated that the concentrations of compound **13d** in the cerebral cortex and plasma

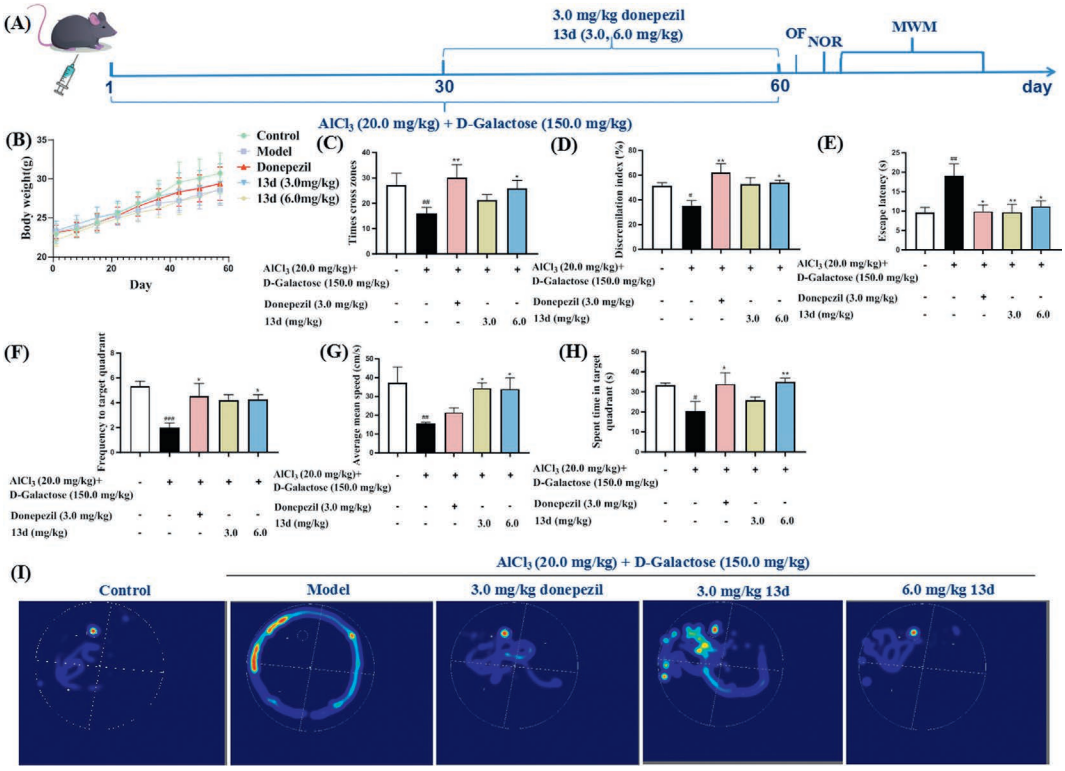


Fig. 4. Effects of **13d** in the $AlCl_3$/D-galactose mice model. Data are presented as mean ± standard deviation (SD) ($n = 9$). (A) The *in vivo* evaluation of **13d** in $AlCl_3$/D-galactose mice. (B) Weight changes were recorded in various experimental groups. (C) The times cross zones were evaluated using the open field test. (D) The discrimination index was evaluated using the novel object recognition test. (E) The spatial exploration escape latency was recorded in various groups using the MWM. (F) The spatial exploration shuttle platform was recorded in various groups using the MWM. (G) Average speeds were recorded in various groups. (H) The quadrant dwell time in spatial exploration were recorded in various groups. (I) Localized cruise heat map were recorded in various groups using the MWM. $^{\#}P < 0.05$, $^{\#\#}P < 0.01$ *vs.* control group; $^{*}P < 0.05$, $^{**}P < 0.01$ *vs.* model group.

for the high dose group was 2.2 ng/g and 45.6 ng/mL, respectively, and B/P ratio was 0.05, demonstrating that compound **13d** presented weak blood-brain barrier permeability.

AD is a chronic, progressive neurodegenerative disorder primarily characterized by memory and cognitive impairments. Currently available clinical medications can only provide temporary symptomatic relief without effectively halting or reversing the progression of AD, highlighting the urgent need for the development of novel anti-AD drugs. Inhibiting PDE4 is considered a promising strategy for the treatment of AD. Herein, we present a novel approach that combines RNN-based fragment generator, virtual screening, and SAR analysis for the *de novo* design of PDE4 inhibitors and the evaluation of their potential anti-AD activity. Our fragment replacement strategy outperforms traditional methods by efficiently exploring chemical space while preserving the α-M scaffold, generating diverse derivatives (>10,000 compounds) with precise modifications—overcoming RNN randomness and scaffold-constrained yield limitations. Based on the natural PDE4 inhibitor α-M, we utilized it as a hit structure to discover a novel PDE4 inhibitor, compound **13d** ($IC_{50} = 72.8$ nmol/L). *In vitro* activity results indicated that compound **13d** exhibited significant anti-inflammatory effects by reducing the levels of NO, IL-6, IL-1β and TNF-α. **13d** also indicated encouraging neuroprotective effects against Glu- and Aβ_{25-35}-induced HT22 cellular injury. Moreover, compound **13d** displayed moderate liver microsome stability ($t_{1/2} = 32.4$ min). *In vivo* experiments demonstrated that **13d** significantly improved the $AlCl_3$-induced zebrafish AD model *via* enhancing cAMP levels by PDE4 inhibition and reducing the levels of inflammatory factors. Additionally, **13d** significantly alleviated $AlCl_3$/D-galactose-induced AD mouse model. Collectively, this study demonstrates the discovery of the PDE4 inhibitor **13d** with anti-AD activity *via* AI, warranting further investigation.

Declaration of competing interest

The authors declare that they have no known competing financial interests or personal relationships that could have appeared to influence the work reported in this paper.

CRediT authorship contribution statement

Zhi-Pei Sang: Writing – review & editing, Writing – original draft, Validation, Project administration, Methodology, Funding acquisition. **Teng Xue:** Investigation, Formal analysis, Data curation. **Qian-Ru Xing:** Visualization, Validation, Methodology, Investigation. **Qi-Yao Zhang:** Methodology, Investigation. **Hong-Song Chen:** Formal analysis, Data curation. **Xue Wang:** Methodology, Investigation. **Fu-Rong Zhang:** Software, Formal analysis, Data curation, Conceptualization. **Wen-Ling Fu:** Validation, Methodology, Investigation, Funding acquisition. **Wu Dong:** Validation, Investigation, Formal analysis, Data curation. **Shu-Heng Huang:** Supervision, Project administration, Methodology, Investigation, Funding acquisition, Formal analysis, Conceptualization. **Yi-You Huang:** Writing – review & editing, Writing – original draft, Validation, Methodology, Investigation. **Hai-Bin Luo:** Writing – review & editing, Supervision, Funding acquisition.

Acknowledgments

This work was financially supported by the National Key Research and Development Program of China (No. 2023YFF1205102);

the National Natural Science Foundation of China (Nos. 22367007, 22377023, and 82304384); the Science Foundation of Hainan Province (Nos. 825MS072, KJRC2023B10 and 824RC500); the China Postdoctoral Science Foundation (No. 2022M712153) and the Fundamental Research Funds for Hainan University (Nos. XTCX2022JKA01, KYQD(ZR)23002).

Supplementary materials

Supplementary material associated with this article can be found, in the online version, at doi:10.1016/j.cclet.2025.111318.

References

[1] R. Hodson, Nature 559 (2018) S1–S2.
[2] S. Long, C. Benoist, W. Weidner, World Alzheimer Report 2023, Alzheimer's Disease International, London, 2023.
[3] J. Zhang, Y. Zhang, J. Wang, et al., Signal Transduct. Target. Ther. 9 (2024) 211.
[4] I. Terao, W. Kodama, Ageing Res. Rev. 94 (2024) 102203.
[5] S. Gauthier, Drugs Aging 18 (2001) 853–862.
[6] Y. Chen, M. Lai, M. Tao, Medicine 103 (2024) e37799.
[7] R.A. Hansen, G. Gartlehner, A.P. Webb, et al., Clin. Interv. Aging 3 (2008) 211–225.
[8] J. Prickaerts, P.R.A. Heckman, A. Blokland, Expert. Opin. Investig. Drugs 26 (2017) 1033–1048.
[9] Y. Wu, Z. Li, Y.Y. Huang, et al., J. Med. Chem. 61 (2018) 5467–5483.
[10] Z. Donders, I.J. Skorupska, E. Willems, et al., Biomed. Pharmacother. 177 (2024) 117009.
[11] H. Wang, F.F. Zhang, Y. Xu, et al., Int. J. Neuropsychopharmacol. 23 (2020) 700–711.
[12] C. Wang, X.M. Yang, Y.Y. Zhuo, et al., Int. J. Neuropsychopharmacol. 15 (2012) 749–766.
[13] H. Guo, Y. Cheng, C. Wang, et al., Neuropharmacology 116 (2017) 260–269.
[14] N. Possemis, F. Verhey, J. Prickaerts, et al., Trials 25 (2024) 162.
[15] M.A. Van Duinen, A. Sambeth, P.R.A. Heckman, et al., Neuropharmacology 131 (2018) 31–38.
[16] T. Chavan, A. Muth, Future Med. Chem. 13 (2021) 1679–1694.
[17] G. Chen, Y. Li, W. Wang, et al., Expert. Opin. Ther. Pat. 28 (2018) 415–427.
[18] A. Yang, C. Liu, J. Wu, et al., Eur. J. Pharmacol. 897 (2021) 173950.
[19] J. Liang, Y.Y. Huang, Q. Zhou, et al., J. Med. Chem. 63 (2020) 3370–3380.
[20] L.S. Franco, B.D.S.M. de Jesus, P.S.M. Pinheiro, et al., Pharmaceuticals 17 (2024) 742.
[21] J.L. Medina-Franco, E. López-López, Expert. Opin. Drug Discov. 19 (2024) 507–510.
[22] D. Paul, G. Sanap, S. Shenoy, et al., Drug Discov. Today 26 (2021) 80–93.
[23] D. Salley, J.S. Manzano, P.J. Kitson, et al., ACS Cent. Sci. 9 (2023) 1525–1537.
[24] Z. Chen, Y. Shi, F. Zhong, et al., Chin. Chem. Lett. 36 (2025) 109956.
[25] Q. Zhou, M. Le, Y. Yang, et al., Acta Pharm. Sin. B 13 (2023) 1180–1191.
[26] Y.Y. Huang, X. Luo, K. Zhang, et al., Chin. Chem. Lett. 36 (2025) 110586.
[27] E.E. Patton, L.I. Zon, D.M. Langenau, Nat. Rev. Drug Discov. 20 (2021) 611–628.
[28] P. Bhattarai, B. Turgutalp, C. Kizil, ACS Chem. Neurosci. 13 (2022) 2939–2941.
[29] A.P. Nadiga, S.K. Krishna, Eur. J. Pharmacol. 965 (2024) 176332.
[30] R. Chen, X. Li, H. Chen, et al., Eur. J. Med. Chem. 251 (2023) 115253.
[31] H. Chen, J. Mi, S. Li, et al., J. Enzyme Inhib. Med. Chem. 38 (2023) 2169682.
[32] Y.H. Chong, Y.H. Suh, Brain Res. 670 (1995) 137–141.
[33] A. Tanas, Ö.Ö. Tozlu, T. Gezmiş, et al., Biomed Res. Int. 2022 (2022) 5467498.
[34] Y. Hu, X. Fang, J. Wang, et al., Neurotoxicology 91 (2022) 60–68.
[35] T. Vishnumukkala, P.K. Gopalakrishna, B. Karikalan, et al., Bioinformation 20 (2024) 508–514.